DOI 10.52209/2706-977X_2025_2_58 IRSTI 55.21.15 UDC 621.914.22

Internal Surface Finish Analysis of Inconel 625 Tube Using MAF and CMAF Processes

Gurpreet Singh*, **Gyanendra Singh, Harish Kumar H**
Chandigarh University, Mohali (Pb.), India
*corresponding author

Abstract. Over time, numerous new alloys and materials were evolved to meet the technological demands of diverse industries. Advanced Nickel based alloys has great demands in many industrial applications such as Marine, solar power plants, Petro-chemical and aerospace due to its remarkable physical properties. Traditional methods of machining and polishing Inconel 625 alloy are difficult because to its outstanding qualities like high hardness and great strength. In present paper, both chemically assisted MAF (CMAF) and magnetic abrasive finishing (MAF) have been utilized to enhance the internal surface finish of Inconel 625 tubes. Utilizing Response Surface Methodology (RSM), experiments have been designed and conducted. The main factors influencing the internal surface finish (PISF) in MAF and CMAF processes are processing time and rotational speed. Results described that CMAF process yields better surface quality as compare to MAF process. Maximum PISF is attained in CMAF at approximately 72%, and in MAF at approximately 59%. Moreover, Surface texture of finished Inconel 625 tubes in MAF and CMAF was also analysed through Scanning electron Microscopy (SEM). Surface finished by CMAF has less scratches, waviness and scratches as compare to surface finished by MAF process.

Keywords: MAF, CMAF, Inconel 625, design expert, surface finish

Introduction

Industries are producing new metals and alloys to meet their technological demands. Inconel 625 alloy finds widespread use in solar power plants, heat exchanger tubing, nuclear power plants, and other applications of a similar nature because of its remarkable qualities [1, 2]. However, because of its greater hardness and toughness, Inconel 625 is hard to cut using conventional methods like turning, milling and grinding [3,4]. To finish hard alloys, researchers have developed some advanced finishing processes. Magnetic abrasive finishing (MAF) is a highly effective technique that is widely used in industry to obtain a precise surface finish with the minimum surface imperfections [5]. It was often used to polish rounded surfaces composed of stainless steel, brass, and aluminum. The inner surface of SUS-304 stainless steel tubes was polished using mixed-type magnetic abrasives and surface roughness descends from 0.7 to 0.2 µm [6]. To polish the inner surface, Yamaguchi and Shinmura [7] utilized MAF with the pole rotation system.

Moreover, Mulik and Pandey [8] enhanced the surface polish by combining MAF with ultrasonic vibration. Further, MAF was used to simultaneously finish the outer and inner surfaces of steel needles and surface finish enhanced around 0.01 µm [9]. Heng et al. [10] finished the SUS-316L tube (Oval shaped) using Al_2O_3/iron-based abrasives, improving the surface polish by about 0.04 µm. Zhang et al. [11] polished the inside surface of the SS316 tube using a brand-new magnetically powered tool in MAF. Yang et al. [12] improved the surface finish from 4.1 µm to 10 nm of thin-walled tube with MAF. Wang et al. [13] suggested nanoparticle-enhanced bonded magnetic abrasive (NEBMA) to enhance the finishing performance of MAF process. Wang et al. [14] investigated MAF process for the finishing of Internal Surfaces of Waveguides fabricated by Selective Laser Melting and improved the surface quality from the roughness of the specimens decreased from Ra 2.5 µm to Ra 0.65 µm. Hence, simple MAF is less productive for hard materials instead of many advantages.

Therefore, the development of chemically assisted MAF (CMAF) aimed to improve MAF's performance with brittle and hard materials. The benefits of chemical machining as well as MAF are combined in CMAF. Initially in CMAF, chemical etching was done on the surface at a higher temperature for a predefined period of time and the workpiece surface layer get diffused due to chemical reaction. The upper surface of workpiece get weakened which is further removed using the MAF method. [15]. Singh et al. [16] used a multi-pole magnetic tool to complete the Inconel 625 tube using the MAF approach. The tungsten flat surfaces were finished using CMAF, and by utilizing ideal settings, the surface polish was increased to about 79.52% [15,17]. Furthermore, Inconel 718 flat surfaces were polished using CMAF, and the results showed that a superior surface finish was achieved at 90 minutes of finishing time, 30% abrasive weight, and 700 gm/lt. of chemical concentration [18]. CMAF was also utilized to concurrently finish the inner and outer surfaces of Inconel 625 tubes. The effects of process parameters were examined and surface finish was enhanced by 72% [19]. Additionally, the effect of CMAF input parameters was examined with regard to Inconel 625 tubes' inner and outer roundness [20, 21]. A genetic algorithm was also tried to optimize the CMAF parameters for surface finish and Material removal [22].

Prior research has documented the use of MAF and CMAF in the finishing of a variety of materials, including nickel alloys, brass, tungsten, and stainless steel. However, there hasn't been much research comparing the performance of MAF and CMAF . Both MAF and CMAF processes for finishing the inner surface of Inconel-625 tubes have been investigated in the current work. The analysis of the performance of MAF and CMAF has involved investigating the effect of input responses on PISF.

1. Materials and Methods

Figure 1 illustrates the MAF and CMAF process principle to finish the inner cylindrical surface. A cylindrical workpiece was kept between the magnet's north and south poles during the MAF process. Both silicon carbide (SiC) particles and iron particles are mixed together as per weight% of abrasives and inserted inside the tube. As magnetic abrasives particles (MAP) align with the lines of magnetic force under magnetic field and MAPs are driven toward the inner surface of the tube. The inner surfaces of the workpiece get polished as the tube rotates and cutting edges of abrasive performs the finishing action.

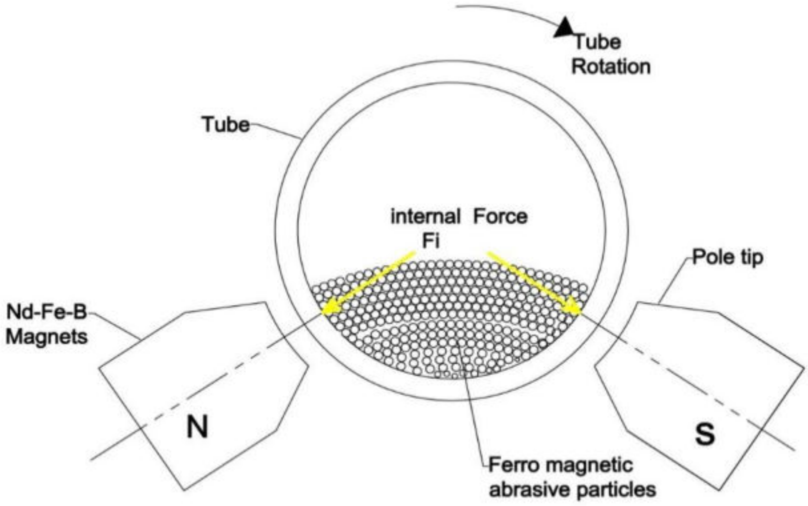

Fig. 1. - Basic finishing principle of MAF and CMAF

CMAF process involves the use of suitable the chemicals on the surface of workpiece. Then chemically treated workpiece is kept in a muffle furnace for 30 minutes at a temperature between 50°C to 65°C. As a result of the etchant's reaction with the work surface, the inner surface layer of the work piece softens throughout this chemical reaction. Further basic MAF principle is used to remove the work surface's soft molecular layer formed chemical etching.

Figure 2 illustrates the finishing setup. The Inconel 625 tube (Ø25 × 2 ×150 mm) inner side was polished using fabricated magnetic tool. Nd-Fe-B magnets (35x35x25 mm) are fastened with two screws on the aluminium fixture. Permanent magnets were used to maintain the constant magnetic flux density (0.5 tesla). An internal yoke composed of SS-400 steel connects the magnets' bottom N-S poles within the aluminium fixture. The outside surface of the tube is positioned parallel to the upper magnet. A multi-speed precision lathe machine was used for the experiments. The smooth rotating motion between the tube surface and the magnet poles is made possible by the PTFE tape that is used to wrap the magnet's poles. The precision lathe machine was equipped with a magnetic tool that used for the experiments.

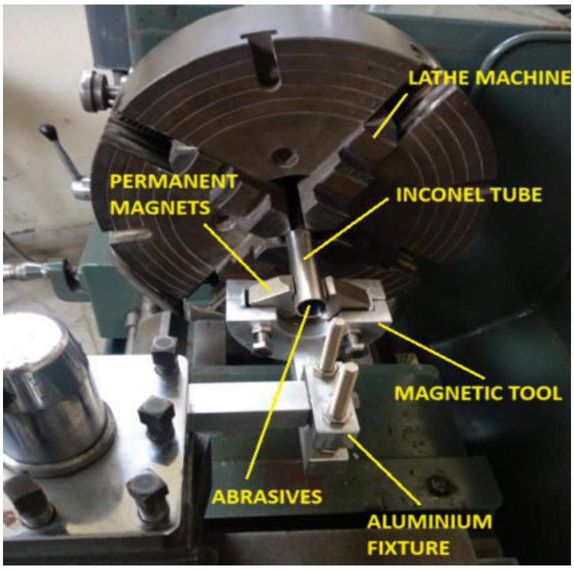

Fig. 2. - Finishing Setup

The input parameters and their range are displayed in Table 1. The range of process factors has been determined based on machine capabilities and reported literature. The three primary input parameters for the MAF and CMAF processes are processing time, abrasive weight percentage and surface rotation speed. Table 2 displays additional constant variables and chemical etching parameters. MAF did not involve any chemical treatment; however, the work surface in the CMAF process was first chemically treated using a chemical solution. The appropriate chemical concentration was taken into consideration when preparing the ethanol and ferric chloride ($FeCl_3$) chemical solution. The tube was placed in an electric muffle furnace after being submerged in the chemical mixture. The temperature was kept at about 65 °C for 30 minutes in order to undergo chemical treatment. The Inconel 625 tubes' top surface diffuses as a result of a chemical reaction. The inside surface layer of tube get soften. Further, MAF is utilized to remove the diffused inner surface layer. The chemically treated tube was positioned between the permanent magnets and 3 gms. of abrasive particles were added inside the tube. The abrasive media get attracted towards the inner surface of tube due to magnetic field lines. Inside the tube, a magnetic abrasive brush was generated which carries out the cutting function. The tube's inner surface get polished as it revolves.

Table 1. - Input factors for MAF and CMAF

S.No.	Input Factors	Designation	Level-1	Level-2	Level-3
			-1	0	1
1	Processing time (Min.)	A	25	50	75
2	Tube rotational speed (RPM)	B	110	190	270
3	Weight % abrasive particles	C	25%	35%	45%

Table 2. Additional parameters

Other Constant parameters	
Specimen	Inconel 625 tubes (Ø25mm x 150mm x 2mm)
Permanent Magnet type	Nd.Fe.B SS-400 yoke Material
Abrasives	Silicon carbide (60 µm)
Iron Particle	300 µm
Chemical treatment parameters in CMAF	
Temperature	65°Celcius
Chemical Name	$FeCl_3$
Chemicals Concentration	600g/lt
Etching duration	30 mins.

Final experiments were planned and executed using Response surface methodology (RSM). It minimizes the time-consuming experiment effort and produces improved correlation between output and input responses. Percentage improvement in surface finish (PISH) is regarded as output response in present work. Telesurf roughness tester was utilized to check the inner surface roughness of Inconel 625 tubes. Average of three readings were considered for the surface roughness measurement. The surface roughness of rough sample ranges from 2.18 µm to 3.88 µm and finished surface using MAF ranges from 1.19 µm to 2.52 µm and finished surface using CMAF ranges from 0.87 µm to 2.10 µm. PISH was determined using the following relation based on surface roughness values for each experiment. Table 3 shows the PISH results for MAF and CMAF under experimental settings.

PISF = (Surface roughness of rough sample – Surface roughness of finished sample)/ Surface roughness of rough sample *100

Table 3. Experimental condition with output responses

Run	A: Processing time	B: Speed (RPM)	C: weight% of abrasives	% improvement in Surface Finish (MAF)	% improvement in Surface Finish (CMAF)
1	75	270	25	53	63
2	50	110	35	30	42
3	25	110	25	11	21
4	50	190	25	40	52
5	50	190	45	49	62
6	50	190	35	45	56
7	75	110	45	37	48
8	25	270	45	23	36
9	50	190	35	34	45
10	75	190	35	31	43
11	25	190	35	19	32
12	50	190	35	38	51
13	50	190	35	39	53
14	50	270	35	59	72
15	50	190	35	34	48

2. Results and Discussion

Results of percentage improvement in surface finish (PISH) in MAF and CMAF processes were analysed using design expert software. Significant models were created for obtained PISH in MAF and CMAF. ANNOVA analysis for PISF in MAF and CMAF are represent ted in Table 4 and Table 5 respectively. The model F-value for PISF in MAF and CMAF are 7.53 and 6.61 respectively. The analysis showed that predicted R^2 value is 0.9318 and 0.9225 respectively in MAF and CMAF model. The adeq. precision value is 9.4 and 9.1 in MAF and CMAF respectively. In order to examine how input factors affect PISH, 3D interaction graphs were plotted which represents the effect of process parameter on the PISF in both processes.

Table 4. ANNOVA table for PISF in MAF

Source	Sum of Squares	df	Mean Square	F-value	p-value	Value
Model	2095.14	9	232.79	7.53	0.0194	significant
A-Processing Time	72	1	72	2.33	0.1875	
B-Speed	420.5	1	420.5	13.6	0.0142	
C-Wt% of Abrasives	40.5	1	40.5	1.31	0.3042	
AB	34.98	1	34.98	1.13	0.3361	
AC	21.16	1	21.16	0.6845	0.4457	
BC	190.41	1	190.41	6.16	0.0557	
A^2	533.34	1	533.34	17.25	0.0089	
B^2	15.89	1	15.89	0.5139	0.5055	
C^2	15.89	1	15.89	0.5139	0.5055	
Residual	154.59	5	30.92			
Lack of Fit	72.59	1	72.59	3.54	0.133	not significant
Pure Error	82	4	20.5			
Cor Total	2249.73	14				

Table 5 ANNOVA table for PISF in CMAF

Source	Sum of Squares	df	Mean Square	F-value	p-value	Value
Model	2129.95	9	236.66	6.61	0.0256	significant
A-Processing Time	60.5	1	60.5	1.69	0.2503	
B-Speed	450	1	450	12.57	0.0165	
C-Wt% of Abrasives	50	1	50	1.4	0.2904	
AB	25	1	25	0.6984	0.4414	
AC	19.3	1	19.3	0.5392	0.4957	
BC	184.74	1	184.74	5.16	0.0723	
A^2	589.38	1	589.38	16.46	0.0098	
B^2	7.86	1	7.86	0.2195	0.6591	
C^2	7.86	1	7.86	0.2195	0.6591	
Residual	178.98	5	35.8			
Lack of Fit	105.78	1	105.78	5.78	0.074	not significant
Pure Error	73.2	4	18.3			
Cor Total	2308.93	14				

3.1 Processing Time and Speed's effect on PISF

The impact of processing time and speed on PISF in MAF is illustrated in Fig, 3 (a) & in CMAF in Fig. 3(b). In both processes, maximum PISF is attained at 75 min. time duration and speed 270 RPM. It has been analyzed that PISF is increasing with the increase in time duration and speed in both processes. It happens because abrasives particles strike rate on work surface is faster at higher speed and finishing duration is also longer. But, It has been observed from plots that PISF in CMAF process greater as compared MAF process. The main reason is the chemical treatment of workpiece. It makes the surface layer softer which is easily to remove using further MAF process.

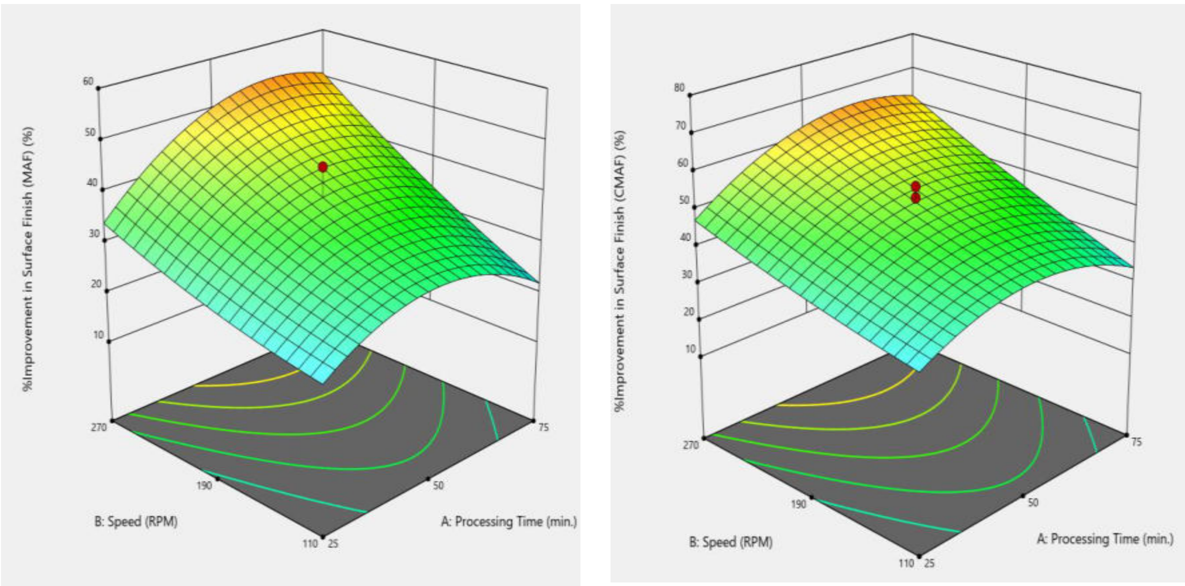

(a) (b)

Fig.3. - Processing time and speed's effect on PISF (a) MAF; (b) CMAF

3.2 Processing Time and Weight% of abrasive's effect on PISF

The impact of time duration and weight% of abrasives in both MAF and CMAF is same as shown in Fig 4(a) and 4(b). PISH is increasing slowly with the increase in weight% of abrasives. At wt% of abrasive 35% and time duration 50 min., the better PISH is attained in both processes. It is also possible to speculate that a magnetic abrasive brush that is more effective was created when the number of cutting edges are increased using the maximum weight percentage of abrasives is 45%. More peaks were removed from surface by using effective magnetic brush for longer duration. If we compare both plots, PISH in CMAF process higher as compare to MAF process due to chemical treatment.

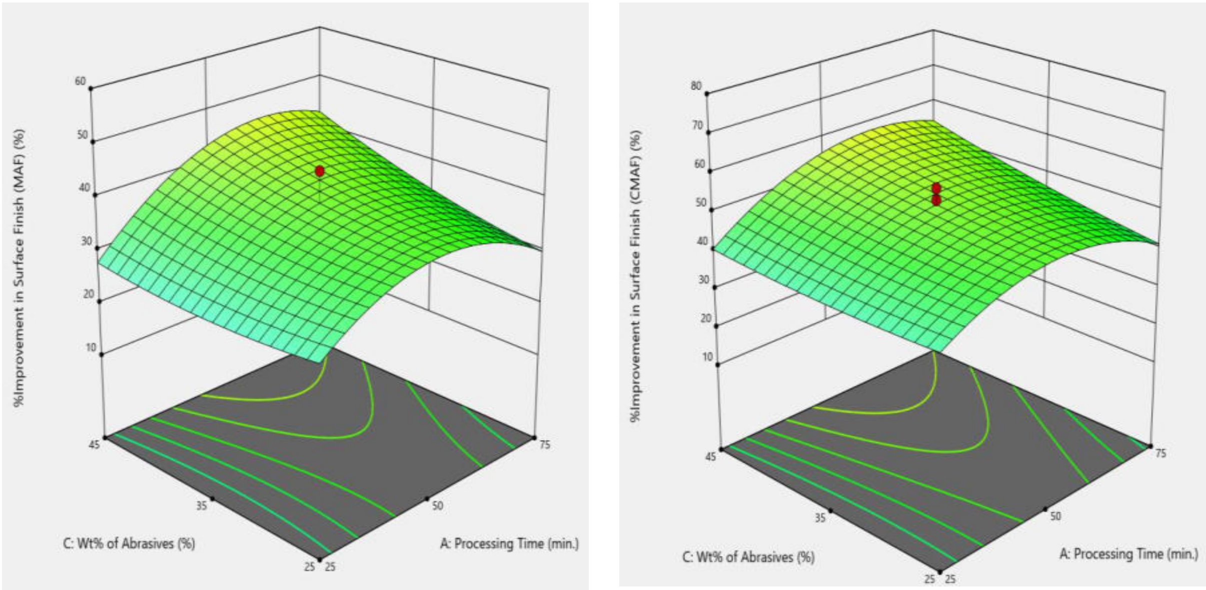

(a) (b)

Fig. 4. - Processing time and weight% of abrasive's effect on PISF (a) MAF; (b) CMAF

3.3 Wt% of abrasives and speed's effect on PISH

The impact of speed and abrasive weight percentage on PISF in the MAF and CMAF processes is shown in Figures 5(a) and 5(b). Maximum PISF is attained in both processes at 25% weight percentage of abrasives and rotational speed of 270 RPM. This occurred as a result of employing the appropriate quantity of abrasive particles and increasing the particle strike rate on the tube surface. The 3D plot comparison also represents that around 70% PISH is achieved in CMAF and around 58% in MAF process.

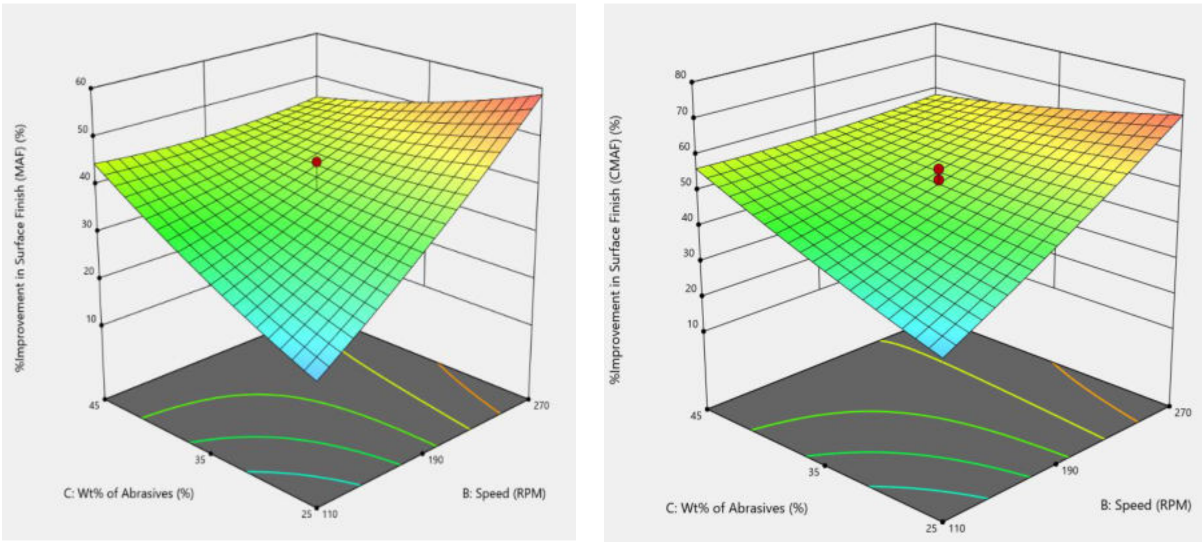

(a) (b)

Fig. 5. - Weight% of abrasives and speed's effect on PISF (a) MAF; (b) CMAF

The result analysis showed that efficiency of CMAF process is better than the MAF process due to chemical treatment of workpiece. The inner surface layer of workpiece gets softer due to chemical reaction and intermolecular bonding of surface becomes weak. This weaken layer can be easily removed by MAF process. The highest processing time and speed is also responsible for improvements in internal surface finish. In CMAF and MAF process, the surface finish improvements is achieved around 72% and 59% respectively. The comparison of surface finish improvements with recently published results represents that our results are remarkable. The comparison summary is given in table 6.

Table 6. Comparison of % improvement in Surface Finish with others

Author	Parameters	% improvement in Surface Finish
Liu and Zou [25]	Rotational speed and time	38%
Shather [23]	Rotational speed, working gap and concentration	34%
Ahmed and Shather [26]	Time, Speed, Particle size, Voltage and Gap	47%
Xie et al [24]	Speed, time and particles size	66%
Present Work	Rotation Speed, Processing Time and Weight % of abrasives	CMAF-72%, MAF-59%

3. Surface Topography

Scanning electron microscopy (SEM) has been used to investigate the surface morphology of finished surfaces by MAF and CMAF, as well as rough surfaces. The rough surface SEM picture is shown in Figure 6(a). The rough surface has imperfections like waviness, scratches, and tool marks etc. Figure 6(b) represents the SEM image of a surface that has been finished using a basic MAF technique. Analysis shows that the surface is not effectively finished using MAF because scratches and lines are visible on the surface. The surface finished by CMAF process is shown in SEM image form in Figure 6(c). It's evident that CMAF surface finishing results in fewer imperfections like scratches, waviness than standard MAF surface finishing. Therefore, it makes sense that, in comparison to the basic MAF process, CMAF offers superior surface finish. The chemical treatment makes the difference which is responsible for better surface finish in CMAF process.

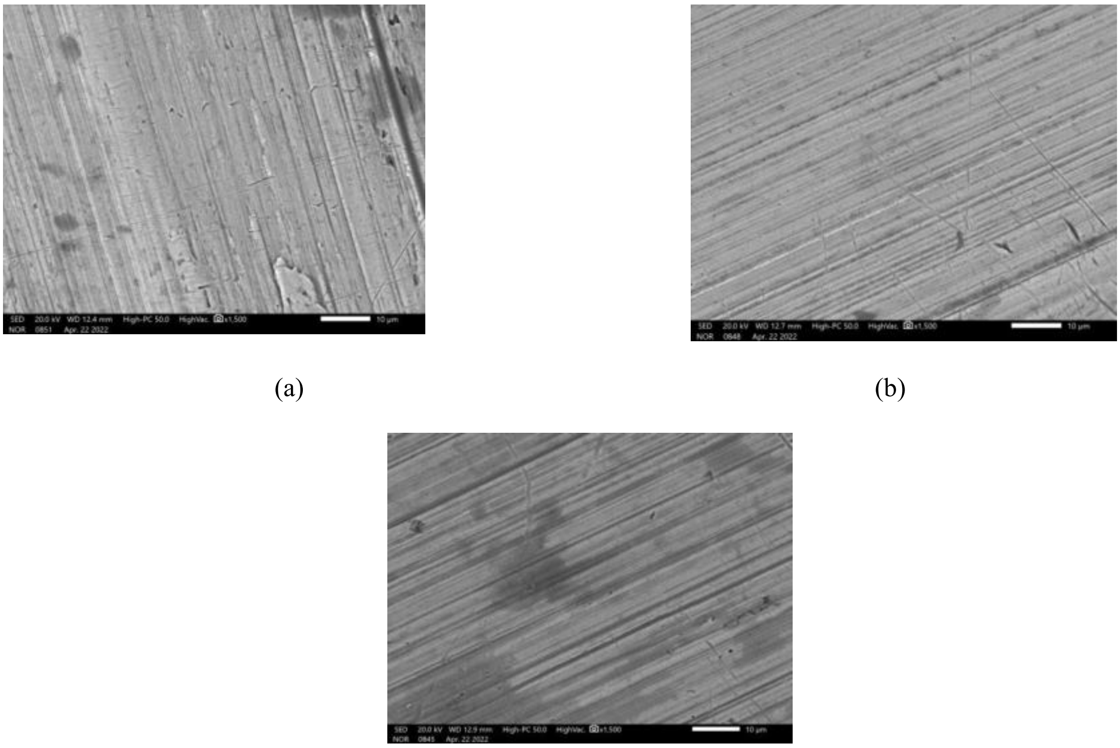

(a) (b)

(c)

Fig. 6. - SEM images (a) Rough sample; (b) Finished with MAF; (c) Finished with CMAF

4. Conclusion

Both MAF and CMAF processes have been effectively utilized to finish the inner surface of Inconel 625 tubes. Investigation points are outlined below:

- The main factors improving PISF in MAF and CMAF are Rotational speed and finishing time. It is suggested to use a 75-min. process duration and 270 RPM in order to achieve maximum PISF in both processes.
- In comparison, CMAF provides better PISF as compare to MAF and maximum PISF 72% in CMAF and 59% in MAF was achieved.
- SEM analysis also justifies that less scratches and imperfections on the CMAF finished surface as compared to MAF finished surface.
- The primary factor enhancing the CMAF process's efficacy is the chemical treatment of Inconel 625 tubes. Efficiency of CMAF is 18% greater than MAF process.

References

[1] Fusova L., Rokicki P., Spotz Z., Saksl K., Siemers C. Tool wear mechanisms during machining of Alloy 625. Adv Mater Res 2011; 275:204–207.

[2] Nath C., Brooks Z., Kurfess T.R. Machinability study and process optimization in face milling of some super alloys with indexable copy face mill inserts. J Manuf Process 2015; 20:88–97.
[3] Dhanabalan S., Sivakumar K., Narayanan C.S. Analysis of form tolerances in electrical discharge machining process for Inconel 718 and 625. Mater Manuf Process 2014; 29:253–259.
[4] Thakur A Gangopadhyay S. State-of-the-art in surface integrity in machining of nickel-based super alloys. Int J Mach Tools Manuf 2016; 100:25–54.
[5] Kala P, Pandey P.M. Comparison of finishing characteristics of two paramagnetic materials using double disc magnetic abrasive finishing. J Manuf Process 2015; 17:63–77.
[6] Shinmura T., Yamaguchi H. Study on a new internal finishing process by the application of magnetic abrasive machining: internal finishing of stainless steel tube and clean gas bomb. JSME Int J Ser C Dyn Control Robot Des Manuf 1995; 38:798–804.
[7] Yamaguchi H., Shinmura T. Study of an internal magnetic abrasive finishing using a pole rotation system. Discussion of the characteristic abrasive behavior. Precis Eng 2000; 24:237–244.
[8] Mulik R.S, Pandey P.M. Experimental investigations and optimization of ultrasonic assisted magnetic abrasive finishing process. Proc Inst Mech Eng Part B J Eng Manuf 2011; 225:1347–1362.
[9] Nteziyaremyea V., Wang Y., Li W., Shihb A. Yamaguchi H. Surface finishing of needles for high-performance biopsy. Procedia CIRP 2014; 14:48–53.
[10] Heng L., Kim J.S, Song J.H, Mun S.D. Application of Al2O/iron-based composite abrasives on MAF process for inner surface finishing of oval-shaped tube: predicting results of MAF process using artificial neural network mode. J Mater Res Technol 2021; 15:3268-3282.
[11] Zhang J., Wang H., Kumar A.S, Jin M. Experimental and theoretical study of internal finishing by a novel magnetically driven polishing tool //Int J Mach Tools Manuf 2020; 1534:103552.
[12] Yang Y., Xue Y., Li B., Fu Y., Jiang Y., Chen R., Hang W., Sun X. A Magnetic Abrasive Finishing Process with an Auxiliary Magnetic Machining Tool for the Internal Surface Finishing of a Thick-Walled Tube //Machines 2022; 10:529.
[13] Wang L., Sun Y., Zhang G., Wu P., Sun Y., Zuo D. Investigation on the preparation and finishing performance of a novel nanoparticle-enhanced bonded magnetic abrasive. Int J Adv Manuf Technol 2023; 129:1523.
[14] Wang L., Sun Y., Xio Z., Yao L., Guo J., Kang S., Mao W, Zuo D. Experimental Investigation on Magnetic Abrasive Finishing for Internal Surfaces of Waveguides Produced by Selective Laser Melting. Materials 2024; 17(7):4631-4642.
[15] Sihag N., Kala N.P., Pandey P.M. Chemo assisted magnetic abrasive finishing: Experimental investigations. Procedia CIRP 2015; 26:539–543.
[16] Singh G., Kumar H., Kumar A. Investigations into Machining of Inconel 625 Flat Surfaces with Multi-pole //Magnetic Tool. Indian J Sci Technol, 2018, 11, 1–9.
[17] Sihag N., Kala P., Pandey P.M. Analysis of Surface Finish Improvement during Ultrasonic Assisted Magnetic Abrasive Finishing on Chemically treated Tungsten Substrate //Procedia Manuf 2017, 10:136–146.
[18] Singh G., Kumar H., Kumar A. Machining of Inconel 718 flat surfaces with chemically assisted magnetic abrasive finishing process //Indian J Sci Technol 2018, 11, 1-6.
[19] Singh G., Kumar H., Kansal H.K, Srivastava A. Effects of chemically assisted magnetic abrasive finishing process parameters on material removal of inconel 625 tubes //Procedia Manuf 2020, 48, 466–473.
[20] Singh G., Kumar H., Kansal H.K. Investigations into internal roundness of Inconel 625 tubes with chemically assisted magnetic abrasive finishing //Mater Today Proc 2019, 19,1579–1585.
[21] Singh G., Kumar H. Influence of chemically assisted magnetic abrasive finishing process parameters on external roundness of Inconel 625 tubes //Mater Today Proc 2020, 37, 3283–3288.
[22] Singh et al. Multiobjective Optimization of Chemically Assisted Magnetic Abrasive Finishing (MAF) on Inconel 625 Tubes Using Genetic Algorithm: Modeling and Microstructural Analysis //Micromachines, 2022,13 (8),1168.
[23] Shather S.K. Enhancement of surface roughness and metal removal rate by using combined abrasives during magnetic abrasive finishing //Int J Res Eng Technol, 2019, 71–8
[24] Xie H. and Zou Y. Investigation on finishing characteristics of magnetic abrasive finishing process using an alternating magnetic field //Machines, 202, 81–17
[25] Liu J. and Zou Y. Study on elucidation of the roundness improvement mechanism of the internal magnetic abrasive finishing process using a magnetic machining tool // J Manuf Mater Process, 2023, 749
[26] Ahmed A. M. S and Shather S.K. Optimizing the five magnetic abrasive finishing factors on surface quality using Taguchi-based grey relational analysis //Eng Res Exp, 2024, 6, 015405.

Information of the authors

Singh Gurpreet, PhD, professor, Mechanical Engineering Department, Chandigarh University
e -mail: garry.dhiman85@gmail.com

Singh Gyanendra, PhD, professor, Mechanical Engineering Department, Chandigarh University
e -mail: gyanendragoindi@gmail.com

Kumar Harish, PhD, professor, Mechanical Engineering Department, Chandigarh University
e -mail: garry.dhiman85@gmail.com

DOI 10.52209/2706-977X_2025_2_66 **IRSTI 55.01.11** **UDC 62-503.56**

Efficient Power Voltage Management of SiC MOSFET at Low Frequencies

Ospanov B.S.[1*], Tatkeeva G.G.[2], Kelesbek N.K.[3]
[1]Abylkas Saginov Karaganda Technical University, Karaganda, Kazakhstan
[2]S. Seifullin Kazakh Agrotechnical University, Astana, Kazakhstan
[3]E.A. Buketov Karaganda University, Karaganda, Kazakhstan
*corresponding author

Abstract. At present, the traditional power sector is undergoing significant changes. A key technology driving these transformations is power electronics, where power quality depends on the transient switching processes of power converters. Currently, commercially available switching devices include Si IGBTs and Si power MOSFETs. Unfortunately, silicon-based technologies are approaching their theoretical limits and are no longer efficient enough to meet modern requirements. This fact has drawn our attention to silicon carbide (SiC), a wide-bandgap semiconductor material. The main objective of this study is the active regulation of the gate voltage applied to the SiC MOSFET to reduce switching losses and electromagnetic interference (EMI) generation. In the conducted experiments, active gate voltage control led to a significant reduction in switching losses-by approximately 35%-compared to fixed gate drive schemes. For example, turn-off energy loss was reduced from 420 µJ to 270 µJ, while the turn-on loss decreased from 510 µJ to 340 µJ. Additionally, by optimizing the gate voltage profile (using techniques such as gate current shaping), the peak EMI voltage measured across the parasitic inductance was lowered by up to 45%, demonstrating a substantial improvement in EMI performance. Rise time was also effectively controlled, reducing from 18 ns to 11 ns, thereby enhancing overall switching speed while mitigating overshoot. These quantitative improvements confirm the effectiveness of dynamic gate control in maximizing the advantages of SiC devices, paving the way for more efficient and reliable power converter designs.

Keywords: Double-pulse test, electromagnetic interference (EMI), silicon carbide (SiC), rise time, case temperature, transistor, full modeling, electron mobility.

Introduction

The research on silicon carbide (SiC) is directly related to materials science, as it focuses on the crystalline structure, thermal and electrical properties of the material, as well as the mechanisms of crystal growth and modification. In particular, the study of SiC polytypism and the selection of the most suitable variant-4H-SiC-for power electronics applications require a deep understanding of phase transitions, crystal lattice defects, and thermal conductivity. These characteristics lie at the intersection of solid-state chemistry, materials physics, and engineering, making this field a clear example of applied materials science in the development of modern semiconductor components.Wide-bandgap semiconductors utilizing silicon carbide (SiC) have become increasingly attractive for power electronics applications due to their superior properties compared to silicon (Si), as reported in studies [1-4]. It is important to note that SiC exhibits polytypism during crystallization, meaning that a single element or compound can form multiple crystalline structures. As a result, various polytypes of SiC exist [5-7]. According to studies [5, 6, 8], the 4H-SiC polytype is the most suitable for power electronics applications. Furthermore, this specific polytype was developed specifically for power electronics applications [5]. Therefore, in this project, the term "SiC" will refer to 4H-SiC.

Three key properties of SiC make it advantageous over Si for high-temperature, high-power, and high-frequency operating conditions [6]: thermal conductivity, critical electric field strength, and bandgap energy.

Table 1. Some Characteristics of SiC & Si [6]

Parameter	Si (Silicon)	4H-SiC (Silicon Carbide)
Bandgap Energy (eV)	1.12	3.26
Critical Electric Field (MV/cm)	0.3-0.4	2.2-2.8
Thermal Conductivity (W/cm·K)	1.5	3.7-4.9
Electron Mobility ($cm^2/V \cdot s$)	1350	800-1000
Saturation Drift Velocity (cm/s)	1.0×10^7	2.0×10^7
Dielectric Constant (εr)	11.8	9.7

This table highlights the superior properties of 4H-SiC compared to traditional silicon, making it a more suitable choice for high-temperature, high-power, and high-frequency power electronics applications.

Silicon carbide (SiC) is a semiconductor material with optoelectronic properties distinct from those of silicon (Si), making it more suitable for high-temperature, high-power, and high-frequency operating conditions. The nearly threefold greater bandgap of SiC means that more energy is required to free an electron from the valence band. Consequently, this results in higher junction temperatures, allowing SiC-based semiconductor devices to operate at significantly higher temperatures.

Additionally, the higher thermal conductivity of silicon carbide ensures more efficient heat dissipation. In practical terms, for the same voltage and current ratings, a smaller heat sink can be used in a SiC-based semiconductor device compared to a silicon-based counterpart. Another advantage of SiC over Si is that the saturation drift velocity of electrons is nearly twice as high. This characteristic enables faster switching speeds, allowing devices to operate at higher switching frequencies.

Overall, these properties lead to reduced passive component sizes in circuit designs, making SiC-based converters more compact and efficient.

1. Methods

To evaluate the switching behavior of a SiC power MOSFET, a double-pulse test (DPT) must be conducted [4, 5, 11]. The switching dynamics can be assessed not only through a standalone double-pulse test circuit but also in the context of its use in power converters [4]. However, as stated in [4], the double-pulse test setup provides more accurate oscilloscope waveforms for current and voltage measurements.

Fundamentally, the test setup is structured as a buck converter supplying an inductive load, as illustrated in the figure below. The DPT circuit is designed to measure key switching characteristics such as turn-on and turn-off losses, voltage and current overshoot, and electromagnetic interference (EMI) generation . By analyzing the waveforms obtained from the test, important performance parameters, including switching speed and energy dissipation, can be precisely evaluated.

The double-pulse test is widely used in power electronics research and industry as a standard method for assessing transient switching performance, particularly for emerging wide-bandgap semiconductors like SiC.

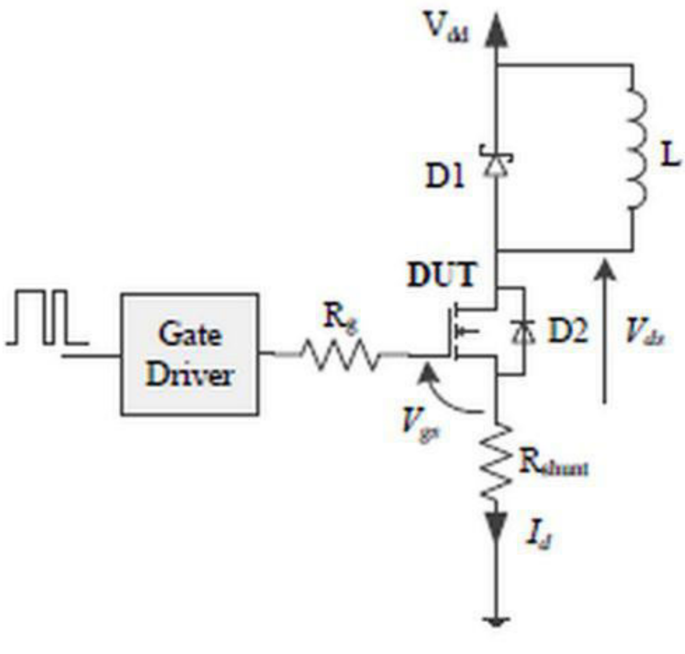

Fig. 1. Double-Pulse Test Setup [11]

In the circuit shown in Figure 1, the MOSFET serves as the Device Under Test (DUT), and its switching behavior is recorded. To generate the necessary turn-on and turn-off signals, the DUT is subjected to two consecutive pulses, where the width of the first pulse is longer than that of the second.

The idealized waveforms obtained during the double-pulse test (DPT), along with the corresponding gate drive pulses, are illustrated in Figure 2 below. These waveforms are essential for analyzing switching losses, transient voltages, and current characteristics of the SiC MOSFET, helping to evaluate its performance under realistic operating conditions.

As shown in Figure 2, the first gate drive pulse is longer than the second one. When the first pulse is initially applied, the MOSFET begins conduction, and the current increases to the desired level. The current value can be adjusted by varying the duration of this first pulse. In other words, the first pulse is modulated to test the Device Under Test (DUT) under different load conditions. Meanwhile, the voltage across the DUT drops as conduction begins.

Once the desired current level is reached, the first pulse ends, and at this moment, the turn-off characteristics of the device are recorded. Upon turn-off, the freewheeling diode enters conduction mode, allowing the inductor current to remain nearly constant at the attained level.

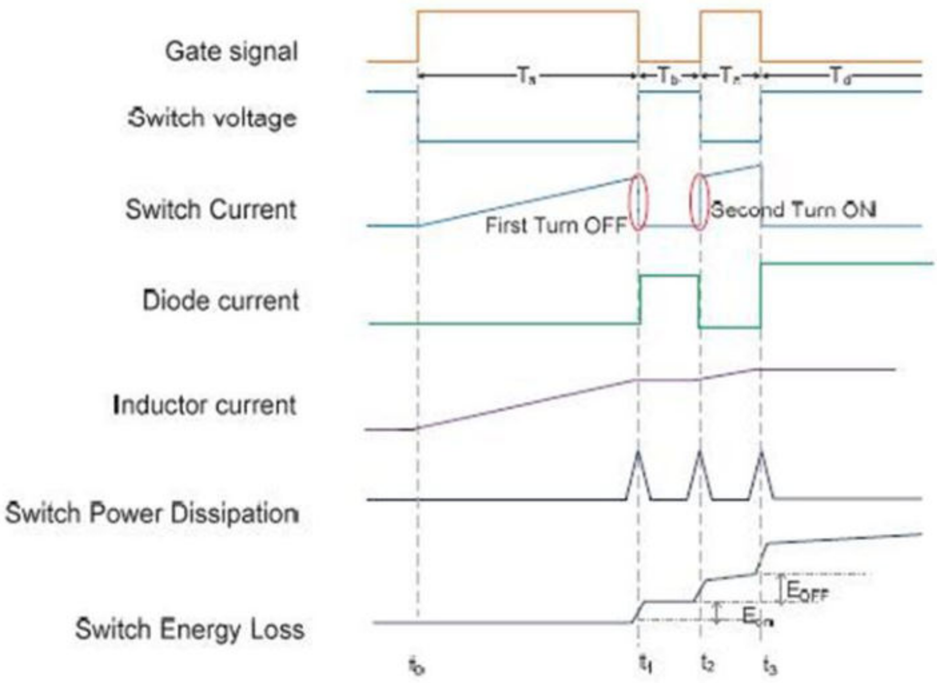

Fig. 2. - Idealized DPT Waveforms [5]

Subsequently, the second pulse is applied causing the current to rise further, while the voltage across the diode decreases at a rate determined by the dv/dt of the MOSFET. This second turn-on transition is used to capture the turn-on characteristics of the switch [9]. Finally, when the second pulse ends, the inductor current gradually decays within the loop formed by the freewheeling diode [10].

Figure 2 also illustrates that most power dissipation occurs during switching transitions (when voltage and current overlap). The switching energy losses are calculated as the integral of power dissipation over the switching transition time, providing critical insights into the efficiency and thermal performance of the MOSFET.

2. Results and discussion

The turn-off characteristics were captured during the falling edge of the gate-off signal. During turn-off, the voltage across the parasitic capacitance C_p decreases from the DC level to zero, resulting in the generation of a discharge current IC_p. Consequently, this peak causes the drain current to decrease until the MOSFET reaches the steady-state off condition. After the turn-off transition, oscillations appear in the current and voltage waveforms. These parasitic oscillations are caused by the interaction of LS,C_p and C_{oss} (the output capacitance of the MOSFET, defined as the sum of CDS and CGD as specified in the datasheet).

Switching signals for different time intervals were obtained here depending on the parasitic inductance, as shown in Table 2.

Table 2. Turn-off signal extraction times for different L_S values

LS	Extraction time when turned on
10 nH	0.3 µs
20 nH	0.4 µs
30 nH	0.525 µs

Table 3 below presents similar characteristics obtained in Table 2, but this time focusing on turn-off transients.

During turn-off, the dV/dt remained relatively unchanged, while the dI/dt showed a tendency to increase, primarily due to the observed current dips. Although the frequency of parasitic oscillations decreased, the drain current settling time increased significantly.

For example, with a parasitic inductance of 10 nH, the settling time was 29.96 ns, whereas at 50 nH, the drain current settled within ±5% in 317.04 ns, which is **more than ten times longer.

Overall, energy losses exhibited an increasing trend due to the prolonged oscillation period; however, these changes can be considered relatively minor.

Table 3. Turn-off transient characteristics for different parasitic inductance values

L_S	dV/dt (kV/μs)	dI/dt (kA/ μs)	$f_{ringing}$ (MHz)	I_d settling time (ns)	Energy (μJ)
10 nH	117.09	4.8094	86.077	29.966	237.63
20 nH	127.32	6.5520	69.119	93.871	249.07
30 nH	125.15	7.6088	62.261	168.68	253.50

Figures 3 to 5 below illustrate the switching transient waveforms for various parasitic inductance (Ls) values using a hard-switching gate drive signal.

From these figures, it is evident that increased parasitic inductance negatively affects the voltage and current waveforms. Specifically, higher Ls leads to:

- Greater voltage overshoot;
- Higher current spikes;
- Increased parasitic oscillations in both voltage and current waveforms;
- Enhanced electromagnetic interference (EMI) generation.

These effects highlight the importance of minimizing parasitic inductance in the circuit layout to achieve efficient and reliable switching performance in SiC MOSFET-based power converters.

.

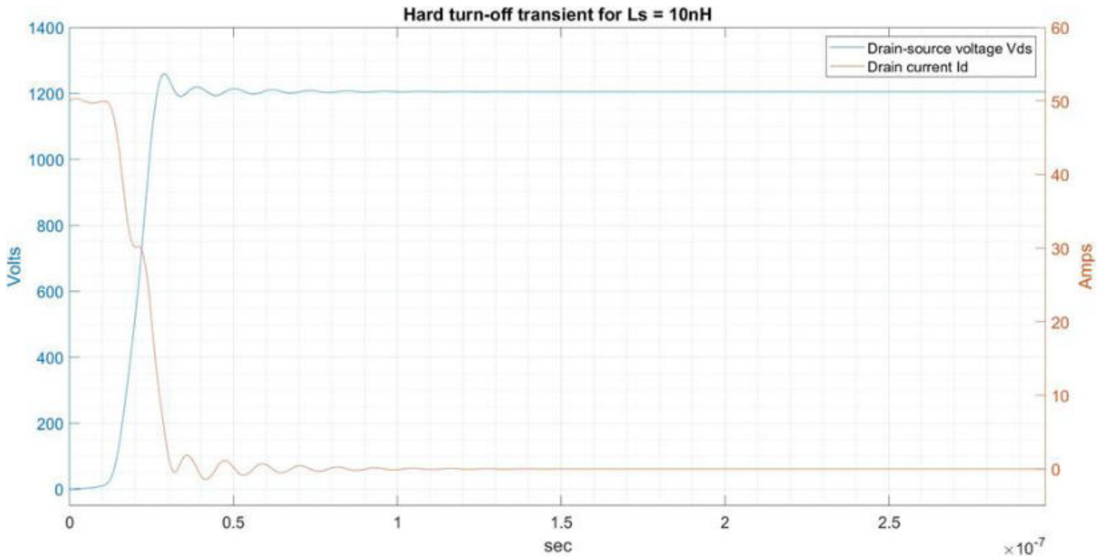

Fig. 3. – Turn-Off Transient Under Hard Switching with Ls = 10 nH

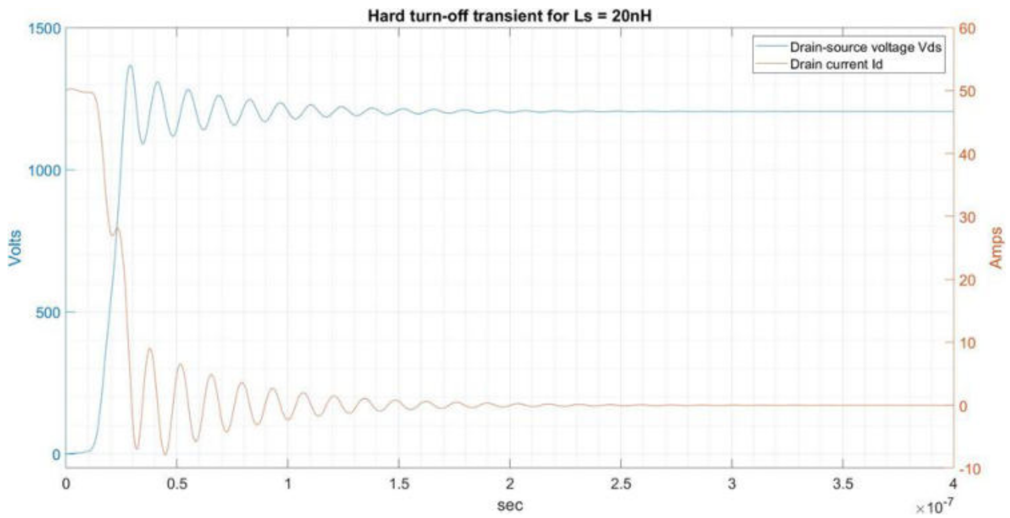

Fig. 4. – Turn-Off Transient Under Hard Switching with Ls = 20nH

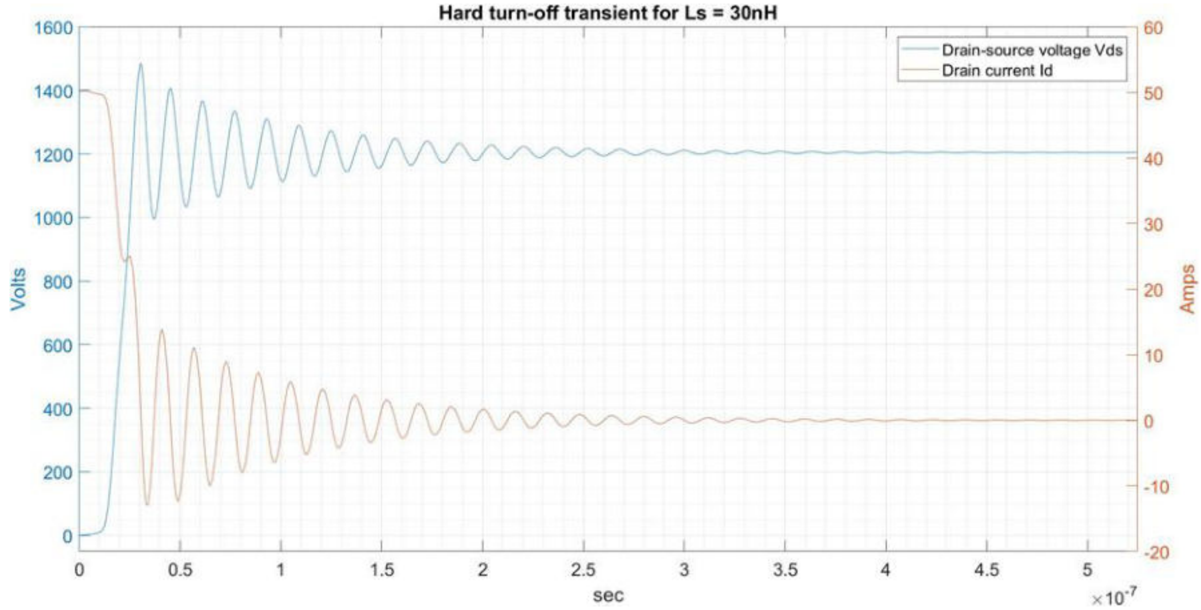

Fig. 5. – Turn-Off Transient Under Hard Switching with Ls = 30 nH

Conclusion

Thus, the double-pulse test (DPT) conducted within an inductance range of 10–30 nH, along with the analysis presented in the graphs, demonstrated the efficiency of SiC MOSFET transistors in power voltage management. The results confirmed that SiC devices offer superior switching performance compared to traditional silicon-based devices, particularly in terms of reduced switching losses, faster switching speeds, and lower electromagnetic interference (EMI). By actively controlling the gate voltage, it was possible to minimize energy dissipation and suppress parasitic oscillations, improving the overall performance and reliability of the system.

Moreover, the influence of parasitic elements such as inductance L_S and capacitances C_p and C_{oss} on switching behavior was clearly observed, underlining the importance of precise layout design and component selection in practical applications. These findings highlight the relevance of SiC technology in modern power electronics, especially for applications that demand high efficiency, compact size, and operation under high-frequency and high-temperature conditions.

Moving forward, we will continue modeling and testing SiC MOSFETs at different switching frequencies, gate driver configurations, and load conditions to determine the most optimal operating parameters. Future work will also focus on implementing these findings in full converter systems and evaluating their real-world performance under varying thermal and electrical stress conditions.

References

[1] Mostaghimi O., Wright N., Horsfall A. Design and performance evaluation of SiC based DC-DC converters for PV applications //IEEE Energy Conversion Congress and and Exposition, 2012

[2] McNutt T., Hefner A., Mantooth H., Berning D., Ryu S. Silicon Carbide Power MOSFET Model and Parameter Extraction Sequence //IEEE Transactions on Power Electronics, 2017, 22(2), 353-363.

[3] Chen Z., Boroyevich D., Burgos R., Wang F. Characterization and modelling of 1.2 kV, 20 A SiC MOSFETs // Proc. IEEE ECCE, 2013, 1480-1487.

[4] Ahmad S. S., Narayanan G. Double pulse test based switching characterization of SiC MOSFET // National Power Electronics Conference (NPEC), Pune, 2017, 319-324

[5] Tiwari S., Abuishmais I., Undeland T., Boysen K. Silicon carbide power transistors for photovoltaic applications //IEEE Trondheim PowerTech, Trondheim, 2011, 1-6.

[6] Tsunenobu Kimoto, 2 - SiC material properties, Editor(s): B. Jayant Baliga, In Woodhead Publishing Series in Electronic and Optical Materials, Wide Bandgap Semiconductor Power Devices, Woodhead Publishing, 2019, 21-42

[7] Rice J., Mookken J. SiC MOSFET gate drive design considerations //IEEE International Workshop on Integrated Power Packaging (IWIPP), Chicago, IL, 2015, 24-27.

[8] Wang J., Liu D., Dymond H. C. P., Dalton J. J. O., Stark B. H. Crosstalk suppression in a 650-V GaN FET bridgeleg converter using 6.7-GHz active gate driver //IEEE Energy Conversion Congress and Exposition (ECCE), Cincinnati, OH, 2017, 1955-1960.

[9] Hazra S., De A., Cheng L., Palmour J., Schupbach M., Hull B. et al. High Switching Performance of 1700V, 50A SiC Power MOSFET over Si IGBT/BiMOSFET for Advanced Power Conversion Applications //IEEE Transactions on Power Electronics, 2015, 1-10.

[10] Wang L., Yang J., Ma H., Wang Z., Olanrewaju K., Kerrouche K. Analysis and Suppression of Unwanted Turn-On and Parasitic Oscillation in SiC JFET-Based Bi-Directional Switches //Electronics, 2018, 7(8), 126.
[11] Helong Li., Munk-Nielsen S. Detail study of SiC MOSFET switching characteristics // IEEE 5th International Symposium on Power Electronics for Distributed Generation Systems (PEDG), 2014.

Information of the authors

Ospanov Bektas Sekerbekovich, M.Sc., Lecturer, Abylkas Saginov Karaganda Technical University
e-mail: bektasss@mail.ru

Tatkeeva Galina Galimzyanovna, D.Sc., Professor, S. Seifullin Kazakh Agrotechnical University
e-mail: tatkeeva@mail.ru

Kelesbek Nabira Kydyrbekkyzy, PhD Student, E.A. Buketov Karaganda University
e-mail: knk_93@bk.ru